RESEARCH PAPER

Electric field effects on current–voltage relationships in microfluidic channels presenting multiple working electrodes in the weak-coupling limit

Nicholas M. Contento · Paul W. Bohn

Abstract While electrochemical methods are well suited for lab-on-a-chip applications, reliably coupling multiple, electrode-controlled processes in a single microfluidic channel remains a considerable challenge, because the electric fields driving electrokinetic flow make it difficult to establish a precisely known potential at the working electrode(s). The challenge of coupling electrochemical detection with microchip electrophoresis is well known; however, the problem is general, arising in other multielectrode arrangements with applications in enhanced detection and chemical processing. Here, we study the effects of induced electric fields on voltammetric behavior in a microchannel containing multiple in-channel electrodes, using a $Fe(CN)_6^{3/4-}$ model system. When an electric field is induced by applying a cathodic potential at one in-channel electrode, the half-wave potential ($E_{1/2}$) for the oxidation of ferrocyanide at an adjacent electrode shifts to more negative potentials. The $E_{1/2}$ value depends linearly on the electric field current at a separate in-channel electrode. The observed shift in $E_{1/2}$ is quantitatively described by a model, which accounts for the change in solution potential caused by the iR drop along the length of the microchannel. The model, which reliably captures changes in electrode location and solution conductivity, apportions the electric field potential between iR drop and electrochemical potential components, enabling the study of microchannel electric field magnitudes at low applied potentials. In the system studied, the iR component of the electric field potential increases exponentially with applied current before reaching an asymptotic value near 80 % of the total applied potential. The methods described will aid in the development and interpretation of future microchip electrochemistry methods, particularly those that benefit from the coupling of electrokinetic and electrochemical phenomena at low voltages.

Keywords Microchannel · Electrochemistry · Electric field · Cyclic voltammetry

1 Introduction

Electrochemistry is well suited for lab-on-a-chip applications due to the low cost of fabricating miniaturized electrodes using modern microfabrication techniques and the relative ease of interpreting electrochemical signals (Nyholm 2005; Wang 2002). As the field of microfluidic electrochemistry has grown, it has become increasingly desirable to perform electrochemical detection in devices that support multiple, independently controlled electrode–solution interfaces, e.g, electrodes for electrokinetic manipulations, chemical generation, or molecular detection. Some applications of multielectrode lab-on-a-chip devices include separation and detection of analytes (Lacher et al. 2001, 2004; Martin et al. 2002), enhancement of electrochemical signals via redox cycling (Ma et al. 2013a, b; Goluch et al. 2009), generating and collecting redox species for kinetic/mechanistic studies (Bitziou et al. 2013; Dumitrescu et al. 2012), and generating molecules needed for miniaturized chemical processing platforms (Contento et al. 2011). Depending on the operating parameters of the device, e.g., electric field strength and

N. M. Contento · P. W. Bohn (✉)
Department of Chemical and Biomolecular Engineering,
University of Notre Dame, Notre Dame, IN 46556, USA
e-mail: pbohn@nd.edu

P. W. Bohn
Department of Chemistry and Biochemistry, University of Notre Dame, Notre Dame, IN 46556, USA

electrode position, significant cross talk can occur between detection electrodes and the secondary electrodes used to either drive electroosmotic flow (EOF) or generate reagents.

Because it does not require large and expensive peripheral equipment like those used for optical or mass spectrometric detection, electrochemical detection is a particularly attractive method for use in microchip capillary electrophoresis devices. Although the use of microchip capillary electrophoresis/electrochemistry has been demonstrated in studies of biologically relevant molecules and biological systems (Hulvey et al. 2010; Bowen and Martin 2009; Nandi et al. 2010), the large electric fields used to drive EOF are the most commonly referenced source of interference in microchannel electrochemical detection (Lu and Cassidy 1994). Indeed, considerable effort has gone into separating detection potentials from separation voltages by either physically decoupling electrodes (Lacher et al. 2004; Chen et al. 2001; Huang and Kok 1995; Joseph Lai et al. 2004) or "floating" the detection electronics (Hebert et al. 2002; Martin et al. 2002). In one interesting approach, field-induced interferences to electrochemical detection are significantly reduced by careful alignment of the detection and reference electrode at the same point in the separation electric field, i.e., at the same point along the length of the microchannel (Kang et al. 2012). While these kinds of ad hoc approaches allow for successful detection in electrified microchannels, a consistent and quantitative framework to describe interactions between electric fields and electrochemical reactions would have substantial value.

Similar signal interferences can occur in other multi-electrode devices designed for applications that do not necessarily include EOF, such as on-chip signal enhancement, kinetic studies, and reaction optimization. Signal amplification can be achieved at closely spaced electrodes by diffusional cycling of electroactive species between a generation and collection electrode (Niwa et al. 1990). This amplification is accomplished in a variety of lab-on-a-chip compatible electrode configurations, including nanogap electrodes (Rassaei et al. 2012), interdigitated electrodes (Lewis et al. 2010), and nanoscale ring-disk electrodes (Ma et al. 2013b). Dual-electrode generation/collection has also been used to study electrocatalysis (Dumitrescu et al. 2012) and homogeneous reaction kinetics (Bitziou et al. 2013) in microfluidic platforms that equal or better the performance of traditional rotating ring-disk electrodes, but with improved scalability. In a similar approach, the generator electrode can be used to generate reagents or pH changes that enable downstream reactions or change the response characteristics of a downstream electrode (Contento et al. 2011; Elsen et al. 2006). When these dual-electrode methods are used in microchip devices, cross talk can arise between the

electric field and the potential driving electron transfer, especially when the potential (or current) is much larger at one electrode than the other, as is typical for electrodes used for EOF or reagent generation.

No practical methods are currently available to quantitatively account for the effects of electric fields and electrochemical processes occurring at adjacent in-channel electrodes. Previous experiments clearly demonstrate that the location of electrodes and the electric field magnitude are important in determining the impact of electric fields on electrochemical detection (Matysik 2000; Forry et al. 2004; Klett et al. 2001). Bipolar electrodes, at which faradaic processes are driven by potential differences between an electrified solution and an electrically floating band electrode, are dependent upon this interaction between electrodes and electric fields (Duval et al. 2003; Squires and Bazant 2004; Dhopeshwarkar et al. 2008; Mavré et al. 2010). Wightman and coworkers proposed an insightful qualitative explanation for the shifts in voltammogram peaks observed during fast-scan cyclic voltammetry at end-channel electrodes coupled to microchip capillary electrophoresis (Forry et al. 2004). Their description of interacting electric fields and electrochemical potentials is similar to that describing bipolar electrochemistry and serves as a point of departure for our work quantifying electric field effects on in-channel electrochemical detection. Quantitation is achieved by monitoring the current passed at the electric field generating electrodes and relating this current to the electric field magnitude via the inherent ionic resistance of microchannels.

Descriptions of microchannel electric fields commonly neglect, or take for granted, the crucial role of faradaic processes occurring at electric field generating electrodes, instead assuming that $\sim 100\%$ of an applied potential is dropped across the length of the microchannel. In reality, the potential at any electric field inducing electrode (FIE), e.g, EOF cathode or generator electrode, is broken into components related to faradaic electron transfer (E_{OHP}) and electric field generation (E_{iR}) such that

$$E_{FIE} = E_{OHP} + E_{iR} \tag{1}$$

where E_{FIE} is the potential applied at the FIE. The two components in Eq. (1) are illustrated in Fig. 1a. E_{OHP} is the potential dropped between the electrode surface and the outer Helmholtz plane (OHP) and drives the electron transfer process (Soestbergen 2012). The potential dropped over the length of the resistive microchannel is E_{iR}. Given the complex nature of the processes that govern the terms in Eq. (1), it is unreasonable to assume a priori a linear increase of E_{iR} with E_{FIE} over the entire available potential range (typically ranging from 0 V to several kV depending on the application). The linearity of EOF velocities with driving potential in capillary electrophoresis suggests that
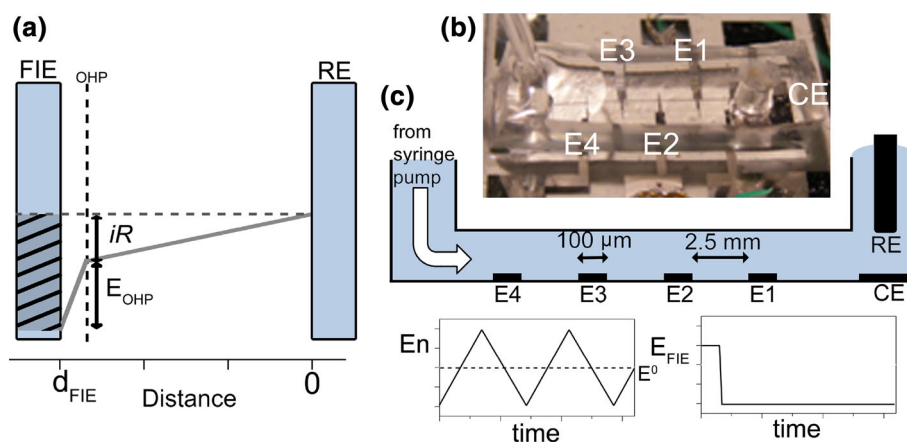
Fig. 1 a Schematic illustration of the components of applied potential, E_{FIE}, which are broken into E_{OHP} and E_{iR}. E_{OHP} is dropped between the electrode surface and the OHP, while E_{iR} is dropped across the microchannel. **b** Image of a microchannel device containing multiple metallic band electrodes. **c** Depiction of the experimental microchannel geometry with flow supplied by a syringe pump from the *left*. A CE and RE are placed in the outlet reservoir, and the electrodes E1–4, which are 100 μm wide and spaced in 2.5 mm increments, are inside the microchannel. *Insets* potential versus time traces for *En* and E_{FIE}

$E_{iR} \propto E_{FIE}$ at large applied potentials; however, there is no guarantee that this linearity holds in all cases, especially when the magnitude of E_{FIE} is small and the relative contribution of E_{OHP} is increased. Recent works involving low-voltage applications in micro-/nanofluidic EOF-coupled electrochemistry (Branagan et al. 2012), electroosmotic pumping (Heuck and Staufer 2011; Xu et al. 2009), and electric field gradient generation (Knust et al. 2013) are examples of applications that would benefit from an improved understanding of the partitioning of applied potentials into faradaic and *iR* drop components for low-voltage electric fields.

Here, we develop a method to quantify electric field effects on electrochemical sensing and study the development of electric fields at low applied potentials. Figure 1b, c shows an image and a depiction of the microchannel electrochemical device, which consists of four 100-μm-wide and one ∼3 mm diameter Au thin-film electrodes patterned on a glass slide. A polymer microchannel overlays the electrodes, allowing solution to be introduced using a syringe pump. An external reference electrode (RE) is placed in the outlet reservoir, which also defines the size of the counter electrode (CE). One of the in-channel electrodes is operated as a FIE, which has a constant cathodic potential applied, while cyclic voltammetry is performed at one of the remaining in-channel electrodes, En ($n = 1–4$). The potential programs for the FIE and En are depicted in the insets to Fig. 1c. A quantitative model is developed to describe the interplay between solution gradients and applied electrode potentials. This model, which captures changes in electrode location and solution conductivity, is also used to study the development of electric fields by measuring the *iR* component of an applied potential at the

FIE via shifts in the electrochemical response at a separate in-channel electrode. This straightforward method provides insight into the fraction of applied potential available for electrokinetic phenomena in a microchannel.

2 Experimental

2.1 Materials

Silicon wafers (*p*-type <100>) were purchased from Montco Silicon Technology. SU-8 2050 photoresist and SU-8 developer were obtained from Microchem. Microchannels were replicated in poly(dimethylsiloxane) (Sylgard 184, Dow Corning). Electrodes were patterned using AZ-5214E (AZ Electronic Materials). Standard microscope slides (VWR) were used as substrates. Potassium nitrate, potassium phosphate mono and dibasic, and potassium ferrocyanide were purchased from Fisher Scientific and used as delivered. Hydrochloric acid (Sigma-Aldrich) was used to adjust the pH of buffered solutions. All ferrocyanide ($Fe(CN)_6^{4-}$)-containing solutions were prepared immediately before use to prevent spontaneous oxidation in solution.

2.2 Device fabrication

Microchannels were fabricated in poly(dimethylsiloxane)(PDMS), using rapid prototyping (McDonald et al. 2000). Briefly, Si wafers were cleaned in an O_2 plasma for 10 min before spin coating a layer of SU-8 2050 photoresist, which was then processed following the manufacturer's instructions for UV exposure and development to achieve a master mold consisting of individual microchannels 55 μm

high, 200 μm wide, and 12 mm long. The height of the microfluidic features was determined by profilometry. PDMS was poured over the completed mold and cured at 75 °C for at least 30 min before channels were cut out for use. A 2-mm circular reservoir was cut in the inlet side of the channel for coupling to a syringe pump via plastic tubing, while a 3-mm circular reservoir was cut in the outlet side of the channel to allow the use of an external reference electrode.

Electrodes were fabricated on glass slides using photolithography and thermal evaporation. Five electrodes were defined using negative-tone AZ-5214E on a glass slide. The electrode pattern consisted of four 100-μm-wide working electrodes and one $\sim 5 \times 5$ mm CE and the necessary contact pads to allow each electrode to be addressed individually. The electrode layout is depicted in Fig. 1c. The slides were then briefly exposed (~ 3 min) to low-power O_2 plasma to remove any residual photoresist. A Cr adhesion layer (4 nm) and Au electrode layer (60–80 nm) were then deposited by thermal evaporation. The remaining photoresist was removed in an agitated acetone bath. The resulting Cr/Au electrodes were then sequentially rinsed in acetone, isopropanol, and DI water and cleaned in high-power O_2 plasma for 10 min prior to device assembly. The PDMS microchannel and electrode-containing glass slide were then exposed to an air plasma for ~ 1 min to promote irreversible bonding between the layers. After bonding of the PDMS microchannel to the electrode-containing glass slide, plastic tubing was inserted into the microchannel inlet and sealed with PDMS, which was carefully coated along the tube–microchannel interface and cured at 75 °C. An image of the completed device is shown in Fig. 1b.
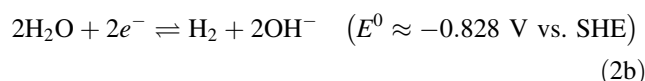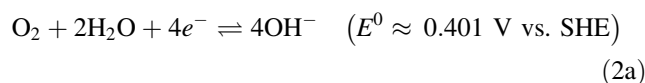
2.3 Flow-channel electrochemistry

A syringe pump was used for the controlled introduction of solutions into the device. Electrochemical experiments were performed using a CHI bipotentiostat (842c, CH Instruments Inc.). The reference electrode in all experiments was Ag/AgCl (69-0053, Warner Instruments). The counter electrode was an evaporated gold disk on the glass slide with its area defined by the size of the outlet microchannel reservoir ($d \approx 3$ mm). Two of the four electrodes, E1–4 in Fig. 1c, were used in each experimental run, with one electrode acting as the FIE, while cyclic voltammetry was performed at the other. The potential of the detection electrode (En) was scanned over a 600–800 mV potential window appropriate to the oxidation of $Fe(CN)_6^{4-}$ at a scan rate of 100 mV/s, while the FIE was either disconnected or held at a constant, cathodic potential. The electrode configurations used in each experiment are described alongside the corresponding results.

3 Results and discussion

3.1 The field inducing electrode (FIE)

Figure 2a depicts a hydrodynamic, microchannel electrode configuration in which electroactive species are detected at one of three interior band electrodes (E1–3), while an electric field is induced across the detection region between the RE at the microchannel outlet and the in-channel FIE. A solution containing $Fe(CN)_6^{4-}$ is driven through the channel. The potential is scanned at one of the interior electrodes E1–3, while the FIE is held at a negative (cathodic) potential, in order to determine the interaction between the electrochemical events occurring at E1–3 and the potential gradients that develop as E_{FIE} increases. This dual-electrode geometry complete with controlled solution flow does not act as an electrochemical generator/collector, because the reversible electroactive species is already in its reduced form when introduced into the channel, and therefore, faradaic processes occurring at the FIE are limited to the irreversible reduction of dissolved oxygen, protons, and water. Eqs. (2a) and (2b), depending upon the magnitude of the applied potential and the solution pH (Eqs. 2a and 2b), are expressed for a neutral/basic solution.

$$O_2 + 2H_2O + 4e^- \rightleftharpoons 4OH^- \quad (E^0 \approx 0.401 \text{ V vs. SHE}) \tag{2a}$$

$$2H_2O + 2e^- \rightleftharpoons H_2 + 2OH^- \quad (E^0 \approx -0.828 \text{ V vs. SHE}) \tag{2b}$$

While future applications are envisioned in which pH changes accompanying the reactions in Eqs. (2a) and (2b) are used to improve microfluidic processes, the oxidation of $Fe(CN)_6^{4-}$ has a negligible pH dependence. The pH insensitivity of the $Fe(CN)_6^{3/4-}$ electrochemistry ensures that any changes in electrochemical processes in the systems studied are only caused by electric fields established by the FIE.

3.2 Shifting $E_{1/2}$

Cyclic voltammograms taken in 1 mM $Fe(CN)_6^{4-}$, 0.1 M KNO_3, and 50 mM phosphate buffer (pH 2.95) at a flow rate of approximately 14 nL s^{-1} (~ 1.3 mm s^{-1} linear flow rate) are shown in Fig. 2b. The CVs display the sigmoidal shape and the absence of reverse (reduction) peaks expected for hydrodynamic band electrodes (Compton et al. 1993). The electrochemical waves maintain their characteristic shape but shift to more negative potentials as the potential at the FIE is poised at more negative values. This shift in the apparent E^0 value is in agreement with the previous observations made
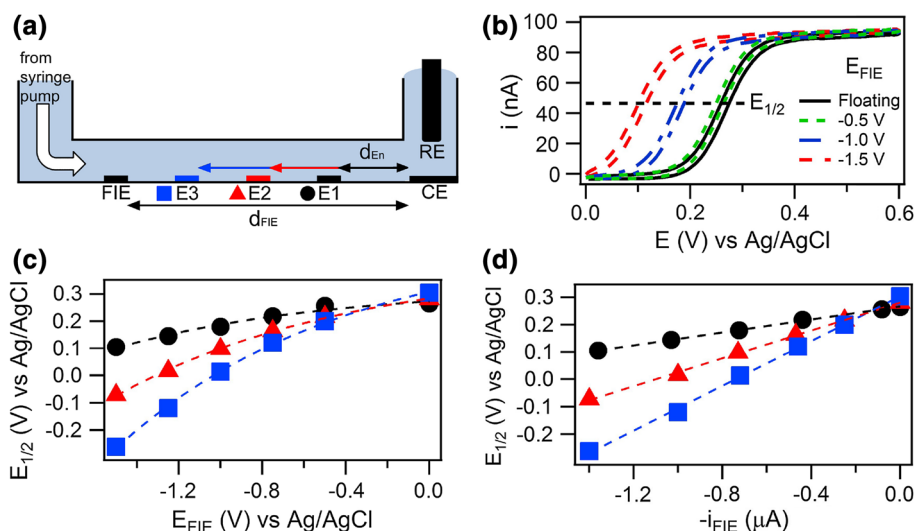
Fig. 2 **a** Schematic illustration of microchannel experiment with the scanned electrodes placed at various positions between the RE and the FIE. **b** Cyclic voltammograms ($v = 100$ mV/s) for 1 mM $Fe(CN)_6^{4-}$ at E1 while E_{FIE} is held at various cathodic potentials. The current obtained at the half-wave potential, $E_{1/2}$, is marked with a dashed line. **c** Values of $E_{1/2}$ as a function of FIE potential. The *dashed lines* are an exponential fit included as a guide to the eye. **d** Values of $E_{1/2}$ as a function of FIE current. The *dashed lines* are fit using Eq. (3). The shapes of the data point markers in panels (**c**) and (**d**) correspond to the shapes next to the electrode labels in (**a**). All solutions contain 50 mM phosphate buffer and 0.1 M KNO_3

during in-channel electrochemical detection in microchip capillary electrophoresis (Forry et al. 2004; Kang et al. 2012). The half-wave potential, $E_{1/2}$, or the potential at which the current is at half its maximum, given by the dashed line in Fig. 2b, is a reliable and easily defined metric for monitoring these shifts. Because there is a slight hysteresis in the CV curves caused by double-layer capacitance, all reported $E_{1/2}$ values are defined at the midpoint between the forward and reverse scans. The effect of the FIE on the electrochemistry is illustrated clearly in Fig. 2c, d, which shows the measured values of $E_{1/2}$ as a function of E_{FIE} or i_{FIE}, respectively, for the three different detection electrode locations.

The value of $E_{1/2}$ has a nonlinear, approximately exponential dependence on E_{FIE}, as seen in Fig. 2c. Slight (~ 20 mV per 2.5 mm of electrode spacing) variations in $E_{1/2}$ at $E_{FIE} = 0$ for the different electrodes are attributed to a small iR drop, which increases as the detection electrode is moved farther from the RE. It should also be noted that the points at $E_{FIE} = 0$ V actually correspond to the condition when the FIE is left floating or disconnected from the bipotentiostat. These points are included for comparison to Fig. 2d, in which the floating/disconnected electrode condition is accurately characterized by having zero current. The dependence of $E_{1/2}$ on E_{FIE} is more pronounced when the scanned electrode is located nearer to the FIE. For example, when $E_{FIE} = -1.5$ V, the $E_{1/2}$ of E3 is approximately -0.25 V while the $E_{1/2}$ of E1 is ~ 0.1 V, where E3 and E1 are 2.5 and 7.7 mm away from the FIE, respectively.

In contrast to Fig. 2c, d reveals a linear dependence ($R^2 > 0.99$) of $E_{1/2}$ on i_{FIE}, which can be fit using an ohmic resistance model

$$E_{1/2} = E_{1/2}(i = 0) + i_{FIE}R^*$$
(3)

where R^* is a resistance fitting parameter with units of Ω and $E_{1/2}$ ($i = 0$) is the half-wave potential at $i_{FIE} = 0$. The factor, R^*, is approximately 118, 255, and 409 kΩ for electrodes E1, E2, and E3, respectively. These fit parameters scale with the distance between the scanned electrode and the RE, i.e., the distance, d_{En}, depicted in Fig. 2a, a dependence that is explored in more detail below. The linearity of $E_{1/2}$ versus i_{FIE} explains the approximately exponential dependence of $E_{1/2}$ versus E_{FIE} seen in Fig. 2c, which is in agreement with the prediction of Butler–Volmer theory that $i_{FIE} \propto \exp(E_{FIE})$. This linearity also suggests that the shifting $E_{1/2}$ values at an arbitrary electrode En are (*a*) linked more directly to the magnitude of the current at the FIE than the applied potential, and (*b*) associated with the resistance of the ionic solutions in the microchannels.

3.3 Electrochemistry in an electric field

To aid in the development of a quantitative model for shifts in $E_{1/2}$, a diagram of the spatial potential distribution in a microchannel containing an arbitrarily positioned detection electrode, En, and a FIE is shown in Fig. 3a. This description ignores the additional potential components related to processes at the counter electrode, a reasonable
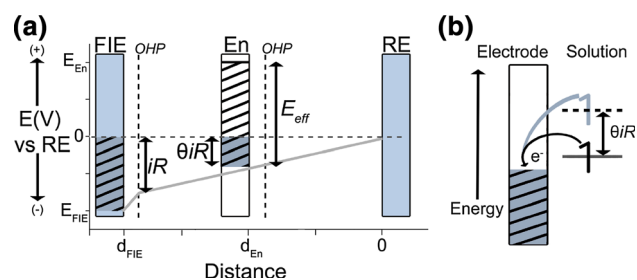
Fig. 3 **a** Potential versus distance in a microchannel where the FIE is held at a negative potential, E_{FIE}, while the scanned electrode is at an oxidative potential, E_{En}, during a CV scan. **b** Energy diagram for the electrode–solution interface when the solution energy is increased by an amount θiR. The *top* of the cross-hatched region corresponds to the Fermi level in the electrode

simplification, because the potentiostat-controlled experiment does not report the total cell potential. Instead, all potentials are referenced to Ag/AgCl. The electrode areas, A, are also purposely designed such that $A_{CE} \gg A_{FIE}$, so that the processes at the CE do not limit electrochemical processes at the FIE. The diagram in Fig. 3a motivates the development of a simple, quantitative framework that allows one either to anticipate the value of $E_{1/2}$ in order to choose an appropriate detection potential or to probe the magnitude of electric fields in microchannels.

In order for heterogeneous electron transfer to occur, a molecule must first reach the edge of the working electrode's OHP, which is represented by the vertical dotted line in Fig. 3a. In a typical macroscale experiment, the majority of the potential applied to an electrode (vs. RE) is dropped over the OHP, providing the driving force for faradaic electron transfer. However, if an electrode is placed in an environment with low conductance, e.g, the resistive microchannels used in this study, a significant fraction of potential drop can occur outside of the OHP (Soestbergen 2012). For the case of a microchannel electrode, this non-faradaic potential drops approximately linearly along the length of the channel, i.e., the iR drop. These two potential drops, one approaching the OHP and the other along the length of the microchannel, are depicted by the solid line in Fig. 3a. While it is difficult to calculate a priori the magnitude of the potential drop up to the OHP, the potential dropped along the length of the microchannel is $\sim iR$, where i is the current through the FIE and R is the microchannel resistance. This iR drop is labeled accordingly in Fig. 3a.

Since iR is approximately linear over the microchannel length, the change in the solution potential adjacent to an electrode placed in this electric field depends on the geometry through a parameter, θ, given by

$$\theta = \frac{d_{En}}{d_{FIE}} \qquad (4)$$

where d_{En} and d_{FIE} are the distances from the RE to the scanned electrode and the FIE, respectively. Since electron

transfer events are ultimately driven by the potential difference between an electrode and the molecules in the adjacent solution, the total effective potential, E_{eff}, at the electrode is the sum of the applied potential, E_{En}, and the offset in the solution potential θiR, given by,

$$E_{eff} = E_{En} + \theta iR \qquad (5)$$

as illustrated in Fig. 3a, or in alternate fashion in Fig. 3b, which shows an energy diagram for the electrode/solution interface. Electrons in the electrode are at the Fermi level dictated by the applied potential (a more positive potential is a lower energy). Electron transfer from the molecular HOMO becomes more energetically favorable when the solution energy is increased by a factor of θiR. This increase in chemical driving force explains the relative ease of the electro-oxidation of $Fe(CN)_6^{4-}$, i.e., the ability to oxidize ferrocyanide at less positive potentials, as i_{FIE} increases.

Since $E_{1/2}$ is a linear function of E_{eff}, Eq. (5) can be extended to calculate the expected change in $E_{1/2}$ with i_{FIE}, which is given by

$$E_{1/2} = E_{1/2}(i = 0) + \theta i_{FIE} R \qquad (6)$$

Equation (6) reveals the physical significance of the fitting parameter used in Eq. (3), i.e., $R^* = \theta R$.

Since $E_{1/2}$ depends on the resistance of the microchannel, the dependence was determined as a function of electrolyte concentration from 0 to 0.5 M KNO$_3$ in 50 mM phosphate buffer with 1 mM $Fe(CN)_6^{4-}$, as shown in Fig. 4. Equation (3) is used to fit the data ($R^2 > 0.99$). As ionic strength, or electrolyte concentration, increases, the channel resistance decreases with $R^* \approx 600, 188, 80$ kΩ for 0, 0.1, and 0.5 M KNO$_3$ and 50 mM phosphate buffer, respectively. The role of channel resistance is especially obvious in the absence of KNO$_3$, for which there is both a very steep slope and a $E_{1/2}(i = 0) \approx 0.38$ V caused by iR drop along the microchannel between the detection electrode, in this case E2, and the RE.
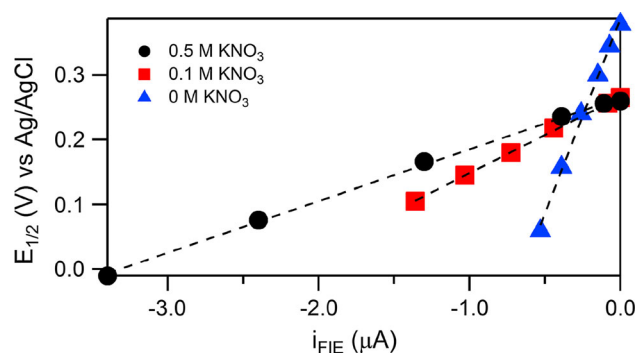
Fig. 4 $E_{1/2}$ versus i_{FIE} for 1 mM $Fe(CN)_6^{4-}$ in 50 mM phosphate buffer and various concentrations of KNO$_3$ as indicated in the legend. The *dashed lines* are fit using Eq. (3)

By considering a first-order approximation for the microchannel resistance, $R \approx (d_{FIE})/A\sigma$, and the geometric definition of θ (Eq. 4), the effect of the electric field on electrochemical measurements, variations in $E_{1/2}$ can be minimized either by placing the detection electrode as close as possible to the RE, a well-known strategy (Klett et al. 2001), or by maximizing the channel cross-sectional area and/or the solution conductivity. Of course, the latter suggestions are of limited utility since the advantages of microfluidic confinement/miniaturization are degraded as A increases and solution conductivity, σ, is inherently limited even at very high electrolyte concentration. When a substantial shift in $E_{1/2}$ is unavoidable, detection potentials or CV scan ranges can be adjusted using Eq. (6) by simply monitoring the current passed through the FIE, whether it is in place to drive EOF or some necessary upstream electrochemical reaction.

3.4 Electrochemistry near an electric field

To determine the effect of placing the detection electrode outside the electric field established between the FIE and RE, an alternate electrode configuration was studied to complement the model illustrated in Fig. 3 and embodied by Eq. (6). In the first alternate configuration, Fig. 5a, the FIE is placed a constant distance from the RE, while CV scans are performed at electrodes E1–E3 placed in the field-free region beyond the FIE. The corresponding $E_{1/2}$ versus i_{FIE} lines are plotted in Fig. 5c. The slope of $E_{1/2}$ versus i_{FIE} is ~ 131 kΩ and is independent of the location of the scanned electrode, d_{En}. Figure 5b shows a second

electrode configuration in which the scanned electrode, now called simply E, is fixed and electrodes FIE1–FIE3 are used to generate electric fields from different points along the channel. In this configuration, an increase in the slope of $E_{1/2}$ versus i_{FIE} is observed as the FIE moves farther from the RE, as seen in Fig. 5d. When fit to Eq. 3, $R^* = 130$, 267, and 385 kΩ for FIE1, FIE2, and FIE3, respectively. The combined results from Fig. 5c, d reveal that the magnitude of the change in $E_{1/2}$ with i_{FIE} is determined only by the distance between the RE and FIE and not the distance between the RE and detection electrode.

The results from Fig. 5 show that when the FIE is placed between the detection electrode and the RE, viz, Fig. 6, the solution potential drops linearly up to the FIE but then remains approximately constant at the value of iR beyond the FIE. In this case, R^* from Eq. (3) is merely the channel resistance between the FIE and RE such that the distance that defines the extent of signal interference is the separation distance between the FIE from the RE, d_{FIE}. Accordingly, interferences can be mitigated by placing the FIE as near to the reference electrode as possible. Alternatively, the appropriate form of Eq. (3) (with $R^* = R_{FIE}$) can be used to correct potential offsets.

3.5 $E_{applied}$ versus iR

Equation (6) can be used directly to determine how the applied potential, E_{FIE}, partitions into faradaic and iR drop components, as depicted in Fig. 1a. The iR component is of primary concern, because it establishes the electric fields
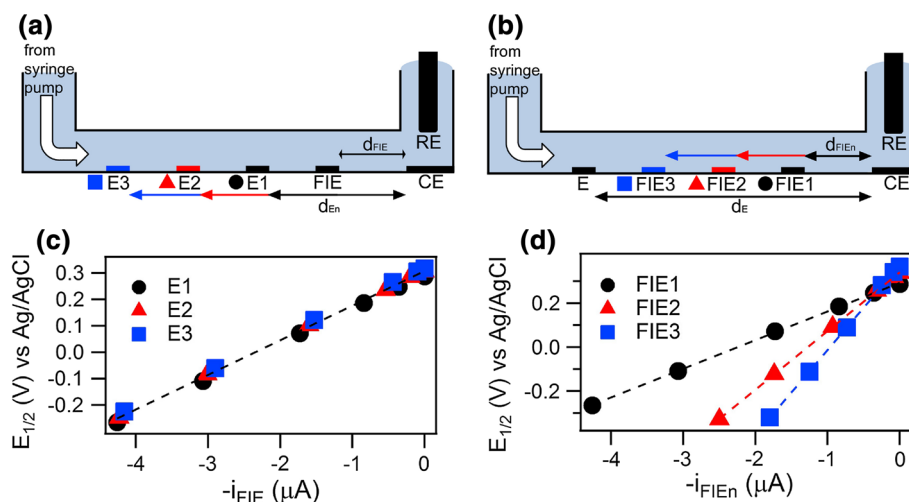
Fig. 5 Electrode configurations in which **a** the FIE is at a constant position between detection electrodes, E1–E3, and **b** the detection electrode, E, is fixed while the FIE position varies. **c** Plot of $E_{1/2}$ versus i_{FIE} for the configuration in panel (**a**). **d** Plot of $E_{1/2}$ versus i_{FIE} for the configuration in panel (**b**). The *dashed lines* are fit to the data using Eq. (3). The shape of the data point markers in (**c**) and (**d**) corresponds to the shapes next to the electrode labels in (**a**) and (**b**), respectively. All solutions contain 1 mM Fe(CN)$_6^{4-}$, 50 mM phosphate buffer, 0.1 M KNO$_3$
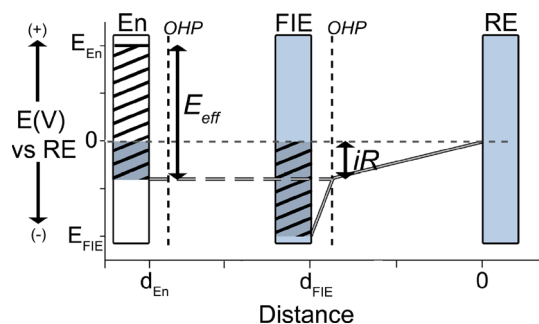
Fig. 6 Potential versus distance in a microchannel in which an FIE is placed between the scanned electrode and the RE and is held at a negative potential, E_{FIE}. An oxidative potential, E_{En}, is applied to the scanned electrode during a CV scan

Fig. 7 Development of iR/E_{FIE} with increasing i_{FIE}. *Dashed line* shows an exponential fit as a guide to the eye

responsible for microchip electrokinetic phenomena. Of particular interest are electric fields generated in channels at low applied potentials, which have recently been used to enhance electrochemical conversion rates in micro-/nano-fluidic structures (Branagan et al. 2012; Gibson et al. 2013) or in low-voltage microchip electrophoresis devices (Xu et al. 2009). These enhancements were attributed to EOF driven by low-voltage electric fields in nanopores ($r \approx 100$–300 nm). The strength of the electric field, F_{EOF}, generated by an electrode is proportional to the iR component of the applied potential, according to,

$$F_{EOF} = \nabla E_{iR} \approx \frac{iR}{d} \tag{7}$$

where d is the electrode separation. A clear description of how the applied potential is partitioned into faradaic (E_{OHP}) and iR (E_{iR}) components is critical to understand the coupling of electroosmotic and electrochemical potentials in channels with high resistance.

In order to probe the relative magnitudes of E_{iR} and the total potential applied at the FIE (E_{FIE}), experiments were performed in the in-field electrode configuration, Fig. 2a, during which potentials as large as -5 V versus RE were applied at the FIE. $E_{1/2}$ was measured at the center electrode, E2, and the value of iR was calculated using Eq. (6) for $E_{FIE} = 0$ to -5 V. This electrode configuration operates at a constant value of $\theta \approx 0.5$. The fraction of the applied potential that takes part in the electric field is plotted, iR/E_{FIE} versus i_{FIE}, in Fig. 7. The fraction of the applied potential that is dropped over the channel increases monotonically up to $i_{FIE} \approx -3.8$ µA, at which point iR/E_{FIE} reaches an asymptotic value near 0.8. These results suggest that at large applied potentials, approximately 20 % of E_{FIE} is responsible for faradaic processes, while the remaining 80 % is available for electrokinetic phenomena. While this ability to probe the partitioning of applied potentials is crucial for understanding low-voltage (low current) electrokinetic applications, the asymptotic
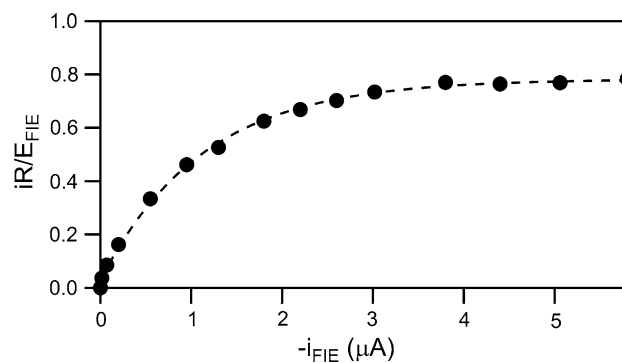
behavior of iR/E_{FIE} versus i_{FIE} also provides interesting insights into the efficiency of microchip electrophoresis methods by demonstrating the microchannel electric field is established by <100 % E_{FIE}.

3.6 The weak-coupling electrode limit

The models depicted in Figs. 3 and 6 assume that the FIE and the detection electrode are only weakly coupled, i.e., that the electric field associated with the detection electrode is negligible compared to that generated by the FIE. This is a reasonable assumption given that $i_E \ll i_{FIE}$, such that the $i_E R$ component of the detection potential is very small compared to $i_{FIE}R$. This is the case for the high electrolyte concentrations used throughout most of this study. The minor offsets of ~ 20 mV in $E_{1/2}$ ($i = 0$) likely reflect the very small $i_E R$ drop related to detection. When operating in 0 M KNO$_3$, Fig. 3, the weak-coupling assumption is less valid.

Clearly, the weak-coupling assumption greatly simplifies the quantitative description of the electronic interactions derived from Figs. 3 and 6. If the potentials at the FIE and detection electrode are strongly coupled, then the electric fields alter the effective electrochemical potentials at both electrodes. This strong-coupling case occurs when the iR drop at the detection electrode, $i_E R$, becomes appreciable in relation to $i_{FIE}R$. This is the topic of ongoing work performed at nanopore-embedded electrodes, which exhibit interesting electrokinetic properties due to large iR effects from high electrochemical currents and large nanopore resistances.

4 Conclusions

When microfluidic channels support multielectrode configurations, constant applied potentials at a field inducing electrode dramatically affect hydrodynamic voltammetry at adjacent in-channel band electrodes. Electrochemical

waves associated with the electro-oxidation of $Fe(CN)_6^{4-}$ were used here to model the shift to more negative potentials, with a linear dependence on the magnitude of the current passed at the FIE. A simple, quantitative description is developed to account for this interaction between microchannel electric fields and electrochemical potentials. The model successfully predicts the effects of changing electrode location and solution conductivity. Aside from being a means to accurately adjust detection potentials in electric fields, the model can also be applied to study the magnitude of the iR drop component of a potential applied at a microchannel electrode. This information about the partitioning of applied potential into faradaic and iR drop components is especially valuable at low applied potentials and provides a blueprint for understanding nanopore electrode structures where electrokinetic and electrochemical potentials become strongly coupled.

References

Bitziou E, Snowden ME, Joseph MB, Leigh SJ, Covington JA, Macpherson JV, Unwin PR (2013) Dual electrode micro-channel flow cell for redox titrations: kinetics and analysis of homogeneous ascorbic acid oxidation. J Electroanal Chem 692:72–79. doi:10.1016/j.jelechem.2012.12.014

Bowen AL, Martin RS (2009) Integration of serpentine channels for microchip electrophoresis with a palladium decoupler and electrochemical detection. Electrophoresis 30(19):3347–3354. doi:10.1002/elps.200900234

Branagan SP, Contento NM, Bohn PW (2012) Enhanced mass transport of electroactive species to annular nanoband electrodes embedded in nanocapillary array membranes. J Am Chem Soc 134(20):8617–8624. doi:10.1021/ja3017158

Chen D-C, Hsu F-L, Zhan D-Z, Chen C-H (2001) Palladium film decoupler for amperometric detection in electrophoresis chips. Anal Chem 73(4):758–762. doi:10.1021/ac000452u

Compton RG, Fisher AC, Wellington RG, Dobson PJ, Leigh PA (1993) Hydrodynamic voltammetry with microelectrodes: channel microband electrodes; theory and experiment. J Phys Chem 97(40):10410–10415. doi:10.1021/j100142a024

Contento NM, Branagan SP, Bohn PW (2011) Electrolysis in nanochannels for in situ reagent generation in confined geometries. Lab Chip 11(21):3634–3641. doi:10.1039/c1lc20570f

Dhopeshwarkar R, Hlushkou D, Nguyen M, Tallarek U, Crooks RM (2008) Electrokinetics in microfluidic channels containing a floating electrode. J Am Chem Soc 130(32):10480–10481. doi:10.1021/ja8036405

Dumitrescu I, Yancey DF, Crooks RM (2012) Dual-electrode microfluidic cell for characterizing electrocatalysts. Lab Chip 12(5):986–993. doi:10.1039/c2lc21181e

Duval JFL, Minor M, Cecilia J, van Leeuwen HP (2003) Coupling of lateral electric field and transversal faradaic processes at the conductor/electrolyte solution interface. J Phys Chem B 107(17):4143–4155. doi:10.1021/jp022459g

Elsen HA, Slowinska K, Hull E, Majda M (2006) Determination of the capacitance of solid-state potentiometric sensors: an electrochemical time-of-flight method. Anal Chem 78(18):6356–6363. doi:10.1021/ac060449w

Forry SP, Murray JR, Heien MLAV, Locascio LE, Wightman RM (2004) Probing electric fields inside microfluidic channels during electroosmotic flow with fast-scan cyclic voltammetry. Anal Chem 76(17):4945–4950. doi:10.1021/ac049591s

Gibson LR, Branagan SP, Bohn PW (2013) Convective delivery of electroactive species to annular nanoband electrodes embedded in nanocapillary-array membranes. Small 9(1):90–97. doi:10.1002/smll.201200237

Goluch ED, Wolfrum B, Singh PS, Zevenbergen MA, Lemay SG (2009) Redox cycling in nanofluidic channels using interdigitated electrodes. Anal Bioanal Chem 394(2):447–456. doi:10.1007/s00216-008-2575-x

Hebert NE, Kuhr WG, Brazill SA (2002) Microchip capillary electrophoresis coupled to sinusoidal voltammetry for the detection of native carbohydrates. Electrophoresis 23(21):3750–3759. doi:10.1002/1522-2683(200211)23:21<3750:aid-elps3750>3.0.co;2-x

Heuck FA, Staufer U (2011) Low voltage electroosmotic pump for high density integration into microfabricated fluidic systems. Microfluid Nanofluidics 10(6):1317–1332. doi:10.1007/s10404-010-0765-2

Huang X, Kok WT (1995) Determination of thiols by capillary electrophoresis with electrochemical detection using a palladium field-decoupler and chemically modified electrodes. J Chromatogr A 716(1–2):347–353. doi:10.1016/0021-9673(95)00447-U

Hulvey MK, Frankenfeld CN, Lunte SM (2010) Separation and detection of peroxynitrite using microchip electrophoresis with amperometric detection. Anal Chem 82(5):1608–1611. doi:10.1021/ac902821v

Joseph Lai C–C, Chen C-H, Ko F-H (2004) In-channel dual-electrode amperometric detection in electrophoretic chips with a palladium film decoupler. J Chromatogr A 1023(1):143–150. doi:10.1016/j.chroma.2003.09.053

Kang CM, Joo S, Bae JH, Kirn YR, Kim Y, Chung TD (2012) In-channel electrochemical detection in the middle of microchannel under high electric field. Anal Chem 84(2):901–907. doi:10.1021/ac2016322

Klett O, Björefors F, Nyholm L (2001) Elimination of high-voltage field effects in end column electrochemical detection in capillary electrophoresis by use of on-chip microband electrodes. Anal Chem 73(8):1909–1915. doi:10.1021/ac0012288

Knust KN, Hlushkou D, Anand RK, Tallarek U, Crooks RM (2013) Electrochemically mediated seawater desalination. Angew Chem Int Ed 52(31):8107–8110. doi:10.1002/anie.201302577

Lacher NA, Garrison KE, Martin RS, Lunte SM (2001) Microchip capillary electrophoresis/electrochemistry. Electrophoresis 22(12):2526–2536. doi:10.1002/1522-2683(200107)22:12<2526:AID-ELPS2526>3.0.CO;2-K

Lacher NA, Lunte SM, Martin RS (2004) development of a microfabricated palladium decoupler/electrochemical detector for microchip capillary electrophoresis using a hybrid glass/poly(dimethylsiloxane) device. Anal Chem 76(9):2482–2491. doi:10.1021/ac030327t

Lewis PM, Sheridan LB, Gawley RE, Fritsch I (2010) Signal amplification in a microchannel from redox cycling with varied electroactive configurations of an individually addressable microband electrode array. Anal Chem 82(5):1659–1668. doi:10.1021/ac901066p

Lu W, Cassidy RM (1994) Background noise in capillary electrophoretic amperometric detection. Anal Chem 66(2):200–204. doi:10.1021/ac00074a004

Ma C, Contento NM, Gibson LR, Bohn PW (2013a) Recessed ring-disk nanoelectrode arrays integrated in nanofluidic structures for selective electrochemical detection. Anal Chem 85(20):9882–9888. doi:10.1021/ac402417w

Ma C, Contento NM, Gibson LR, Bohn PW (2013b) Redox cycling in nanoscale recessed ring-disk electrode arrays for enhanced electrochemical sensitivity. ACS Nano 7(6):5483–5490. doi:10.1021/nn401542x

Martin RS, Ratzlaff KL, Huynh BH, Lunte SM (2002) In-channel electrochemical detection for microchip capillary electrophoresis using an electrically isolated potentiostat. Anal Chem 74(5):1136–1143. doi:10.1021/ac011087p

Matysik F-M (2000) Experimental characterization of end-column electrochemical detection in conjunction with nonaqueous capillary electrophoresis. Anal Chem 72(11):2581–2586. doi:10.1021/ac991326x

Mavré Fo, Anand RK, Laws DR, Chow K-F, Chang B-Y, Crooks JA, Crooks RM (2010) Bipolar electrodes: a useful tool for concentration, separation, and detection of analytes in micro-electrochemical systems. Anal Chem 82(21):8766–8774. doi:10.1021/ac101262v

McDonald JC, Duffy DC, Anderson JR, Chiu DT, Wu HK, Schueller OJA, Whitesides GM (2000) Fabrication of microfluidic systems in poly(dimethylsiloxane). Electrophoresis 21(1):27–40. doi:10.1002/(SICI)1522-2683(20000101)21:1<27:AID-ELPS27>3.3.CO;2-3

Nandi P, Desai DP, Lunte SM (2010) Development of a PDMS-based microchip electrophoresis device for continuous online in vivo monitoring of microdialysis samples. Electrophoresis 31(8):1414–1422. doi:10.1002/elps.200900612

Niwa O, Morita M, Tabei H (1990) Electrochemical behavior of reversible redox species at interdigitated array electrodes with different geometries: consideration of redox cycling and collection efficiency. Anal Chem 62(5):447–452. doi:10.1021/ac00204a006

Nyholm L (2005) Electrochemical techniques for lab-on-a-chip applications. Analyst 130(5):599–605. doi:10.1039/B415004J

Rassaei L, Mathwig K, Goluch ED, Lemay SG (2012) Hydrodynamic voltammetry with nanogap electrodes. J Phys Chem C 116(20):10913–10916. doi:10.1021/jp2118696

Soestbergen M (2012) Frumkin-Butler-Volmer theory and mass transfer in electrochemical cells. Russ J Electrochem 48(6):570–579. doi:10.1134/s1023193512060110

Squires TM, Bazant MZ (2004) Induced-charge electro-osmosis. J Fluid Mech 509(1):217–252

Wang J (2002) Electrochemical detection for microscale analytical systems: a review. Talanta 56(2):223–231. doi:10.1016/S0039-9140(01)00592-6

Xu Y, Hu XG, Liang J, Sun JX, Gu WW, Zhao TM, Wen ZY (2009) A microsystem of low-voltage-driven electrophoresis on microchip with array electrode pairs for the separation of amino acids. Anal Bioanal Chem 394(7):1947–1953. doi:10.1007/s00216-009-2889-3